Journal of Materials Chemistry C

Accepted Manuscript

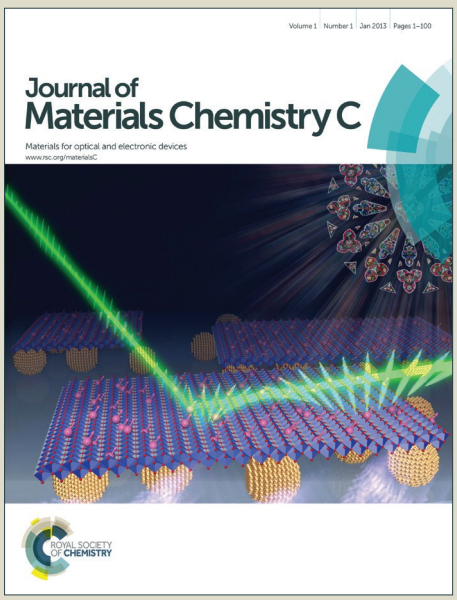

ROYAL SOCIETY OF CHEMISTRY

www.rsc.org/materialsC

Journal of Materials Chemistry C

RSCPublishing

ARTICLE

$CuMo_{0.9}W_{0.1}O_4$ phase transition with thermochromic, piezochromic, thermosalient effects

Cite this: DOI: 10.1039/x0xx00000x

Received 00th January 2014,
Accepted 00th January 2014

DOI: 10.1039/x0xx00000x

www.rsc.org/MaterialsC

L. Robertson[a,b], N. Penin[a,b], V. Blanco-Gutierrez[a,b], D. Sheptyakov[c], A. Demourgues[a,b], M. Gaudon[a,b,*]

$AMoO_4$ compounds (A = Co, Mn, Fe, Ni, Cu, or Zn) exhibit a first-order phase transition associated with piezochromic and thermochromic phenomena, as demonstrated in previous works. In this study, neutron diffraction patterns were collected for $CuMo_{0.9}W_{0.1}O_4$ samples across the hysteresis cycle to accurately characterize the structural evolution (i.e., cell parameters and atomic positions) versus temperature. This study provides information regarding the phase-transition origin. In accordance with the Birch-Murnaghan model, the phase transition is due to the higher compressibility coefficient, despite the presence of the shorter bonds for the high-temperature form. The cell-volume difference of 13% between the high and low temperature forms leads to additional exotic properties: the thermosalient effect ("jumping crystals") associated with a certain crystallite fracture (along the -101 plane) is shown.

1. Introduction

The temperature- or pressure-induced color change in $CuMoO_4$-type compounds originates from a first-order transition between two structural forms [1-11]. The structural characterization of the two allotropic forms (both triclinic with *P-1* space group) at room temperature from X-ray data was firstly proposed by Ehrenberg et al., from Darmstadt university [10]. The pressure-temperature diagrams of the three various allotropic forms of the head-member $CuMoO_4$ compound were proposed the same year (1997) by the same group [5]. Important remark is that the high-temperature form is greenish, whereas the low-temperature one is brownish. Hence, these authors were also the firsts reporting spectroscopic investigation on the optical switch associated with pressure-induced phase transition on the $CuMoO_4$ composition [4,9]. The thermo- and piezo-chromism phenomena associated with this type of phase transition can be then considered of great interest for applications as thermal sensors [12-14] or shock sensors [15-17]. The works previously performed by our group [18-21] have shown that the compound $CuMo_{0.9}W_{0.1}O_4$, among the $CuMo_{1-x}W_xO_4$ series, is very interesting because a 100°C hysteresis between T1/2 up and T1/2 down (from the high- to the low-temperature phase transformation during heating and from the low- (γ-form) to high-temperature form (α-form) during cooling, respectively) is observed, i.e., its color changes from brown to green by warming at 360 K and from green to brown by cooling at 275 K. For this end-member composition, which was shown to be the one with the maximal tungsten doping rate within *P-1* triclinic solid solutions [19], the hysteresis loop occurs near room temperature, leading to several applications because both allotropic forms are stable at room temperature/room pressure. For instance, this property leads the possibility to change the color in a nonreversible way from green to brown by applying a weak pressure (e.g., a finger push) [20]. From these previous works [19-21], a general scheme showing the optical behavior of $CuMo_{0.9}W_{0.1}O_4$ powder under the influence of temperature is reported in **Figure 1**, which also shows the unit cell projection of the high- and the low-temperature phases along the b axis. This phase transformation, which involves a latent heat release and results in an abrupt change in volume, is characteristic of a first-order phase transition.

This phase transformation was described as "pseudo-reconstructive" [5], because (i) it is a non-diffusive transition, for which the path matrix is the identity matrix and the atomic displacements are less than 1/10 Å; and (ii) the breaking and reconstruction of bonds can occur, depending on the reaction side. The molybdenum environment in the two phases is significantly different: in the low-temperature phase, Mo is surrounded by six oxygen anions (5 +1 distances) to form octahedral sites, whereas in the high-temperature phase, Mo is surrounded by four oxygen anions to form tetrahedral sites and presents the lowest density.

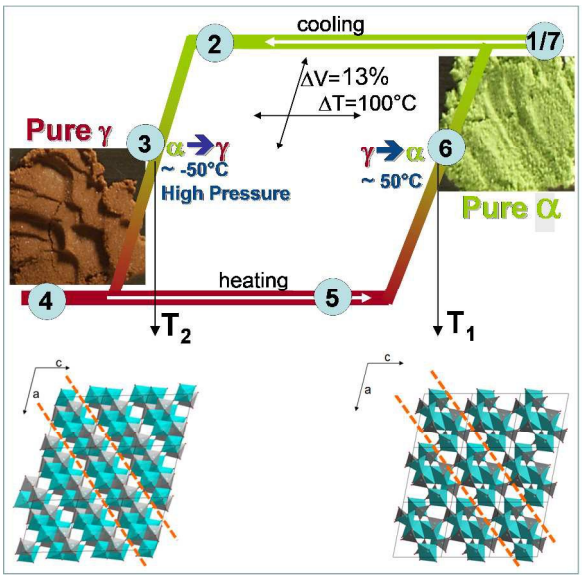

Fig.1. Phase transition description for the compound $CuMo_{0.9}W_{0.1}O_4$. The figure shows both crystalline structures along *b* cell axis projection, photographs of the corresponding powder, and the characteristic temperatures of the phase transition hysteresis loop.

In this paper is proposed an accurate investigation of the structural parameters evolution, including cell parameters and oxygen anions positioning versus temperature from neutron diffraction, recorded all along the hysteresis loop descriptive of the phase transition. The results are used to calculate the reticular energy curves versus temperatures of the low and high-temperature allotropic forms. Especially, the large cell expansion/contraction at the phase transition is discussed in regard of its interesting physical consequences opening new window for this compound as thermosalient sensor or actuator.

Methods

All Samples were prepared by the solid-state route employing stoichiometric amounts of Cu_2O (or Co_3O_4, NiO and MgO for the last part) and MoO_3 and WO_3 single oxides as reactants. After homogenization of the reactants mixture by grinding in an agate mortar, the powder was placed in an alumina crucible to be thermally treated under air in two steps. First, the mixture was treated at 400°C for 10 h (dwell time), with a 1°C/min heating rate and then, after re-homogenization of the mixture by grinding, a second step was given at 700°C for 10 h with the same heating rate.

The neutron powder diffraction experiments were carried out at the high-resolution powder diffractometer HRPT [22] at Paul Scherrer Institute (Villigen PSI) between room temperature and T = 2K, using λ = 1.494 Å wavelength. The powder samples (≈ 5 g) were loaded into vanadium cylinders of 8 mm inner diameter. The low-temperature measurements were performed using a He cryostat, whose contribution to the total scattering was minimized using an oscillating radial collimator. All profiles and structures refinements were carried out using the FULLPROF suite package [23].

Photographs from optical, scanning, and transmission microscopes are also here proposed. The optical microscope used is a Leica IM1000 multifocus in reflective mode. For scanning electronic microscopy (SEM) analysis, we used a Field Emissive Gun - Scanning Electronic Microscope (FEG-SEM) in order to characterize the crystallite as well as the crystallite morphology (shape, size and special rearrangement) on which the spatial resolution can be estimated at about 1 nm. Transmission Electron Microscopy (TEM) was performed on a TECNAI F20 equipment with a Field Emissive Gun (FEG), operating at 200 kV and with a point resolution of 0.24 nm.

The Madelung term of the reticular energies is hereafter calculated using an ionic model approach derived from Madelung Theory. This theory, based on a point charge model (formal charge considering a purely ionic system), takes into account the potential of every site of the crystal lattice in order to respect the oxidation state of each element. The calculation of the reticular energies was made using a program developed in 1990 based on the Ewald approximation [24] (Ewald summation). For each calculation, this program requires the complete crystal structure parameters, i.e., the lattice parameters and the atomic positions. The Ewald summation allows only the calculation of the Madelung term of the reticular energies; the repulsive contribution is not taken into account.

The pressure was applied in a uniaxial way following the details described in previous studies [18-19]. The powder samples were introduced in a pellet-dye with a varying diameter from 6 to 13 mm depending on the desired pressure. The pressure was applied thanks to a home-built scalepan balance in which a counter mass was used in a lever system with a pivot point in order to multiply the mechanical force (effort) that can be applied on the piston of the pellet matrix. For the actuator applications evaluation the same set-up was used, the materials is then heated during the process by a heating device equipped with a temperature regulation.

Results and Discussion

Analysis of the consequences of the phase transition on the structural parameters was performed using *in-situ* neutron diffraction. In particular, neutron diffraction was preferred over X-ray diffraction to solve the difficulty related to the positioning of the oxygen anions: there are 12 distinct general positions, with three x, y and z coordinates for each position, which must be refined. The refinements are complex due to the large number of refined parameters, but they are robust. As illustration, for one allotropic form (whatever the γ-form or the α-form), 12 background parameters, 4 peak profile parameters, 6 cell parameters (triclinic group), and the following atomic positioning: 18*3 atomic coordinates, and 3 groups of isotropic displacement factors (the same 1st displacement for all the Cu^{2+} ions, a 2nd one for all the other Mo^{6+} and W^{6+} cations , and at least the 3rd one for all oxygen ions) were refined. An additional difficulty is that both the forms are detected all along the hysteresis cycles. Indeed, low-temperature form "pollutes" a bit the samples at high temperature, and reciprocally, high-temperature form remains as minor phase at low temperature. Typical Rietveld refinement results and the associated

reliability factors are presented for the illustration for both the α and γ-forms in **Figure 2**. The wt% of the α and γ-forms, the cell parameters and the cell volume obtained at various temperatures are also reported in the **table1**.

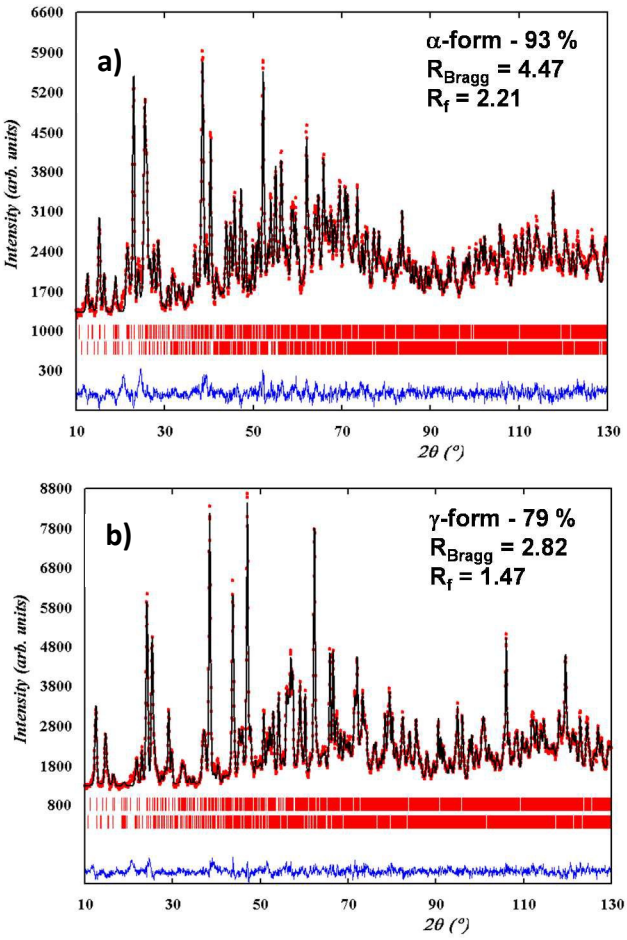

Fig.2. Neutron diffraction refinement patterns on powder samples showing mixtures of the α-form and the γ-form obtained at 400 K (a) and 200 K (b).

Table 1. Unit-cell parameters at various temperatures for both the α-form and γ-form extracted from neutron diffraction

T° (K)	wt %	a (Å)	b(Å)	c(Å)	α (°)	β (°)	γ (°)	V_{cell}(Å^3)
α form								
470	92	9.9136	6.7947	8.3765	101.14	96.83	107.04	**525.6**
400 (cool)	93	9.9113	6.7954	8.3726	101.14	96.85	107.04	**525.2**
350 (cool)	91	9.9072	6.7975	8.3661	101.14	96.89	107.05	**524.7**
250 (cool)	54	9.9049	6.7995	8.3631	101.15	96.92	107.05	**524.5**
200 (cool)	20	9.9017	6.8030	8.3606	101.13	96.97	107.04	**524.4**
400 (heat)	69	9.9093	6.7948	8.3724	101.13	96.87	107.04	**525.5**
γ form								
200 (cool)	80	9.7114	6.3125	7.9760	94.74	103.22	103.27	**460.5**
67	92	9.6987	6.3138	7.9591	94.74	103.07	103.27	**460.5**
100 (heat)	93	9.7050	6.3135	7.9631	94.74	103.15	103.27	**460.9**
200 (heat)	93	9.7124	6.3128	7.9766	94.74	103.22	103.27	**461.8**
300 (heat)	93	9.7208	6.3139	7.9870	94.74	103.34	103.28	**462.6**
400 (heat)	31	9.7254	6.3142	7.9960	94.75	103.44	103.29	**463.2**

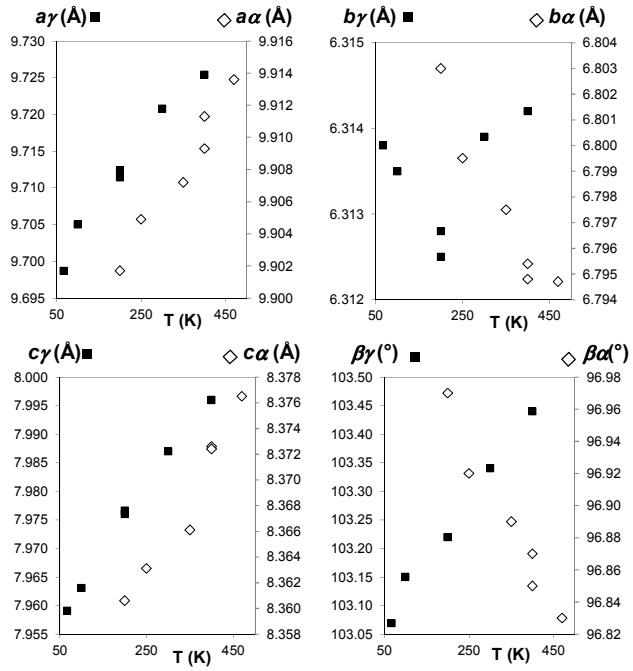

Fig.3. Variation in the *a*, *b*, *c* and β unit-cell parameters versus temperature for both the α-form and γ-form extracted from neutron diffraction.

The evolution of the cell parameters *versus* temperature for both the α and γ-forms is reported in **Figure 3.** The α-form was analyzed during the cooling step between points 1 and 3 reported in the cycling process drawn in **Figure 1**, and the γ-form was analyzed for the cooling or heating step, i.e. between points 3 and 6. The analyses performed on points 3 and 6 - respectively at 200K during cooling and 400K during heating step - show the occurrence of a biphasic domain allowing the exploitation of the refinement results for the both phases in cohabitation. As already shown from magnetic reflective spectroscopy measurements on the same sample in a previous study [19], the biphasic domain, i.e. the transition temperature range, extends approximately over a temperature range of 100K at approximately 200K in the cooling step and 350K in the heating step, respectively. The very high number of diffraction peaks for the two triclinic forms does not allow the accurate atomic positioning in the biphasic domain. Nevertheless, it must be noted that in the range of coexistence of the two phases, the peak profiles are not broadened in comparison to those in the monophasic domains. This means that the advancement of the phase transformation is clearly not due to a progressive growth of the forming phase. At this step, our interpretation is that the progressivity of the transformation is due to the wide crystallite size distribution. Indeed, it has already been shown that the crystallite size influences the temperature of the phase-transition parameters [18]. A last diffraction pattern analysis was performed after the end of one complete cycle (point 7). No significant change (of the cell parameters and atomic positions of the obtained α-form) is observed between the analysis performed on points 1 and 7. The *a* and *c* cell parameters exhibit monotonic expansion *versus* the increase in the temperature for the two allotropic forms, whereas the *b* parameter evolution is more specific (see **Figure3**). Indeed, for the high-

temperature form, the *b* parameter shows a contraction with increased temperature. Furthermore, for the low-temperature form, this *b* cell parameter first decreases *versus* temperature and then expands at a higher temperature with a change in the behavior at approximately 200 K. It can be proposed from these results that the weakest bonds of the structure are parallel to the *b*-axis, considering that the softest bonds (the most ionic ones) are adaptable to the atomic displacements linked to the thermal expansion of the hardest bonds (the most covalent ones). The global expansion of the cell volume supports this explanation.

Moreover, it is possible to extract the volume thermal expansion of the two allotropic forms from the temperature dependence of the unit-cell parameters: $2.1\text{x}10^{-5}$ K^{-1} and $0.9\text{x}10^{-5}$ K^{-1} for the low- and high-temperature forms, respectively, i.e., a twofold higher thermal expansion for the γ-form than for the α-form. This can be explained by the Mo-O bonds: the Mo-O bonds in the γ-form with the Mo^{6+} ion in an octahedral site are weaker than the Mo-O bonds of the α-form with the Mo^{6+} in a tetrahedral site (more covalent). Hence, the latter is more rigid and less subject to atomic vibration. Additionally, the cell-volume variation between the two forms for a constant temperature is approximately 13%: the cell volumes are equal to 463 and 525 $Å^3$ for the γ-form and α-form, respectively, at 300 K, a temperature for which the two phases are stable since this temperature is in the middle of the hysteresis loop.

The atomic position refinement using neutron diffraction data enables the calculation of the reticular energy and evolution *versus* the temperature for the two allotropic forms. The two basic models used for the reticular energy calculation of ionic ceramics are the Born-Lande and Born-Mayer models, which are distinguished by different definitions of the repulsive term. Considering the reticular energy (E_r) function of the Madelung energy (E_M) (i.e., defined hereafter as the electrostatic attractive term of the reticular energy: $E_M = (A \cdot Z^+ \cdot Z \cdot N_a \cdot e^2)/(4 \cdot \pi \cdot \varepsilon_0 \cdot r_0)$ with A as the Madelung constant for the structure), (i) $E_r = E_M \cdot (1 - 1/n)$, where n is the Born exponent in the Born-Lande model; and (ii) $E_r = E_M \cdot (1 - \rho/r_0)$, where ρ is the compressibility factor, and r_0 is the representative bond distance between neighboring ions in the structure, in the Born-Mayer equation. In the Born-Lande model, the exponent n is tabulated for all atomic elements, and the calculation of the n parameter for a structure depends on the stoichiometric composition. For instance, the calculation for the compound $CuMo_{0.9}W_{0.1}O_4$ leads to n = 6.53; n_O = 5, n_{Cu} = 9, n_{Mo} = 10, and n_W = 12. In the Born-Mayer model, the ρ compressibility factor is inversely proportional to the bulk modulus, *e.g.*, the characteristic of the softness of the structure. E_M was calculated in the first step thanks to the Ewald method from all of the atomic positions. This process is derived from a program developed in 1990 based on the Ewald approximation [24]; the method is based on a point-charge model (for which the formal charge considers a purely ionic system), taking into account the potential of every site of the crystal lattice to reflect the oxidation degree of each element. For each calculation, this program requires the complete crystal structure parameters: the lattice parameters and the ion positions. The Ewald summation enables only the calculation of the Madelung term of the reticular energies; the repulsive contribution is not considered.

The attractive term of the reticular energy is clearly lower for the high-temperature form than for the low-temperature one, regardless of the temperature range. Thus, this observation is in opposition with the phase transition experimentally observed; i.e., only the high-temperature transition should occur. It was hypothesized that the repulsive contribution should be different enough to compensate for the attractive-term gap. Taking for the Lande coefficient the theoretical value (n_γ = 6.53) for the low-temperature form, the Lande term for the high-temperature form (n_α) can be calculated for input into the calculation, which leads to a crossing of the reticular energy at approximately room temperature (e.g., at approximately the T_0 temperature at the center of the hysteresis-transition cycle) and should be equal to 5.7. This is shown in **Figure 4**. This means that the occurrence of a higher repulsive contribution ($1/n$) for the α-form is approximately 15% higher than for the γ-form. The calculation is relevant, considering the Born-Mayer relation. Indeed, the α-form exhibits shorter r_0 bonds (lowest coordination sites) as well as higher compressibility (because the α-form exhibits the lowest density). The addition of these two effects should therefore lead to a ratio ρ/r_0 that is much higher than for the low-temperature form. In summary, the occurrence of this type of remarkable first-order phase transition for a $CuMoO_4$-type compound is due to the combination of a high attractive term and a high repulsive term for the high-temperature form, compared to those of the low-temperature form.

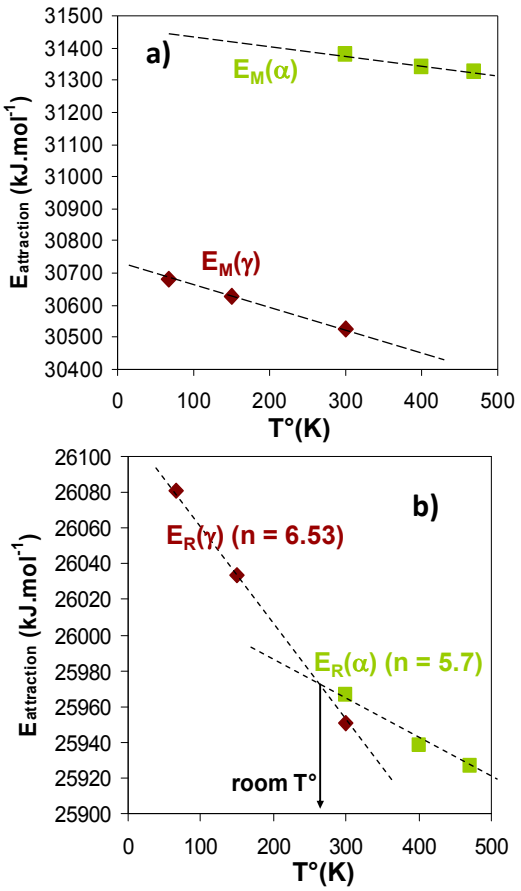

Fig.4. Attractive term of the reticular energy (a) and the reticular energy (b) versus temperature deduced from atomic positions for the two allotropic forms..

To complete the discussion, the simplest plausible dependence of energy on volume for a solid (Birch-Murnaghan model [25-27]) can also be presented. In this model, the reticular energy on both sides of equilibrium: (reticular energy: E_0; volume: V_0) can be described by a quadratic parabola *versus* the phase volume:

$$E_r(V) = E_0 + 9/8\ V_0B_0[(V_0/V)^{2/3}\text{-}1]^2 + 9/16\ B_0(B_0\text{'}\text{-}4)V_0[(V_0/V)^{2/3}\text{-}1]^3,$$

where V is the cell volume, B_0 is the bulk modulus, and B_0' is its pressure derivative. Considering that B_0' is ~4 in these systems, the equation can be simplified to:

$$E_r(V) = E_0 + 9/8\ V_0B_0[(V_0/V)^{2/3}\text{-}1]^2.$$

Moreover, considering the dependence of the volume on temperature: $V = V_0 + \alpha\ V_0\ T$, where α is the volume thermal expansion coefficient (K^{-1}), another equation for the dependence of the reticular energy on temperature can be obtained:

$$E_r(T) = E_0 + 1/2\ (\alpha)^2B_0(T)^2/V_0.$$

It was shown from neutron diffraction analyses that the α-form exhibits an α coefficient twice that of the γ-form. Furthermore, from the respective densities, it can be deduced that the γ-form bulk modulus is largely higher than the α-form bulk modulus and that the Vo equilibrium volume is largely lower for the γ-form than for the α-form. The temperature-dependence term of the reticular energy (i.e., $½B_0(\alpha)^2/V_0$) is also higher for the low-temperature form. Hence, at 0 K, if the γ-form is the stable one, the phase transition must occur at a higher temperature since the reticular energy curves would cross at the transition point. The curves are simulated on the **Figure 5**.

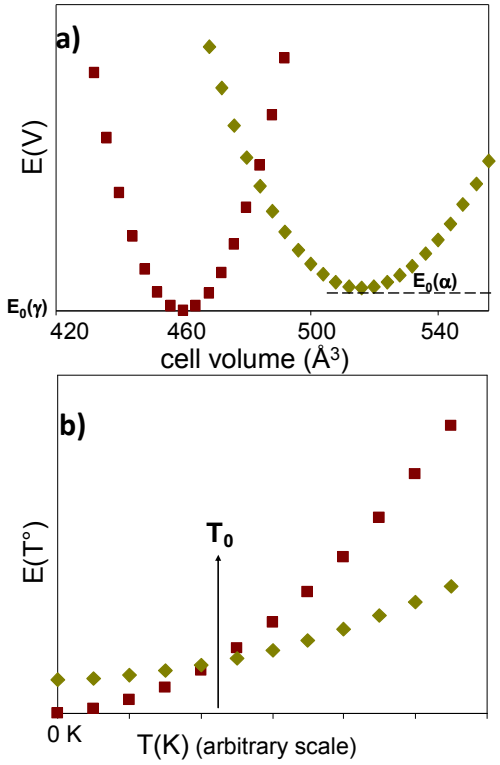

Fig.5. Evolution of the reticular energy from the Birch Murnagahn mode for the two allotropic forms versus cell volume (a) and temperature (b).

The last section discusses the morphological modifications occurring at the phase transition and its consequences observed with scanning electronic and optical microscopies. First, it can be noted that both half transitions (in the cooling and heating modes) are spread over ~100 °C (see also [20-21]). This can be interpreted as the consequence of the large width of the crystallite size distribution and/or a progressive germination-growth mechanism. The neutron diffraction analyses performed here have previously shown that, in the biphasic range of temperature, regardless of the mode, both of the phases always exhibit very narrow peaks. There was no indication of the presence of nano-germs and their progressive growth *versus* temperature through the phase transition. Observation under an optical microscope has enabled clarification of the situation. The half-transition studied was that of the cooling mode (with a transformation from the α to the γ-form); the transition was initiated by the deposition of liquid nitrogen droplets on a glass slide onto which the oxide powder is also deposited. This observation shows that, during the transition (during the coexistence of the two phases), a very sharp transition ("instantaneous") affects all of the crystallites (at least in micrometer-scale areas): this is demonstrated by red flashing lights (γ crystallites) that appear suddenly among the green crystallites (**Figure 6a**). One of very interesting effects of such a "rapid-domino transition" is that a "thermosalient" phenomenon also occurs [28-30]. Indeed, certain crystallites move their positions during the transition, and the immediacy of the transition produces forceful jumps of the crystals (marked by squares in the **Fig.6b - 6c**).

The thermosalient effect has only been reported for organic crystals. The diffusionless phase transformations can be divided into two categories: one dominated by shuffles and one dominated by lattice distortion-induced phase transformations. Clearly, the $CuMoO_4$-type compounds exhibit a phase transition that belongs to the second category. This category can be divided again into two subcategories with a dominant expansion phenomenon or deviatometric distortion (as exhibited by the martensitic transformations used in shape-memory alloys). Clearly, the $CuMoO_4$-type compounds exhibit a phase transition classified in the second subcategory. To the best of our knowledge, the $CuMo_{0.9}W_{0.1}O_4$ compound is the only inorganic specimen that exhibits this type of first-order transition associated with a large thermal expansion. Recognizing the phase-transition behavior and its association with thermosalient effects, we can imagine new applications for $CuMoO_4$-type compounds as thermal actuators. Although, the lack of elasticity of the ceramic bonds in comparison with the metallic ones in shape-memory alloys, could be a limitation. Even if the transformation mode is a diffusionless mode, all of the atomic displacements are infinitesimal in regard to the small change of their reduced coordinate changes and the immediacy of the propagation of the unit-cell contraction from cell to cell on the scale of the entire crystallite produce drastic constraints. These constraints allow the thermosalient effect but unfortunately also produce "chemical fracturing" of the largest crystallites.

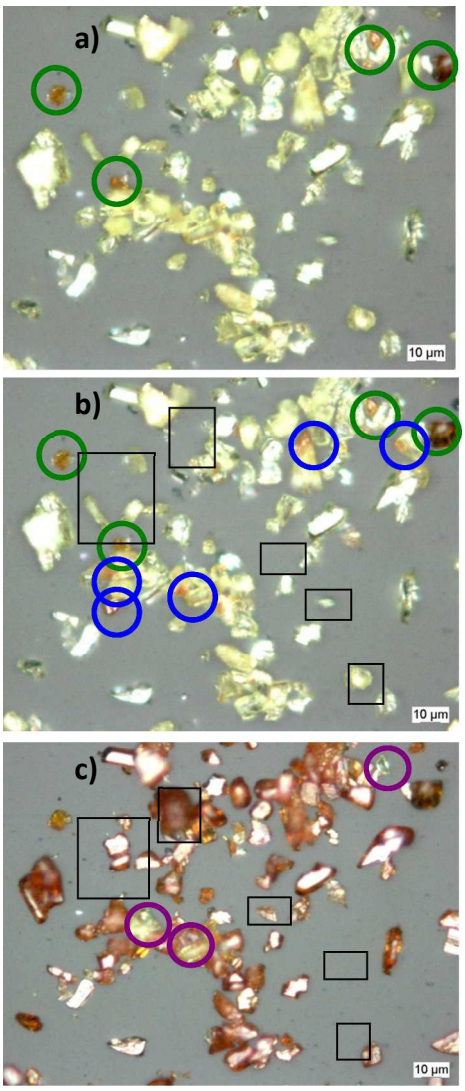

Fig.6. Phase transition from the α-form to the γ-form followed with an optical microscope. (a) The phase transition has just started (the brown crystallites are shown by green circles), (b) The phase transition induces certain crystallites to turn brown (blue circles), (c) The phase transition is nearly complete (the last green crystallites are shown by purple circles) and jumping crystals (displaced or missing crystallites) are evidenced by black rectangles.

The SEM photographs reported in **Figure 7** show the morphology of a fresh powder (high-temperature form) and a powder that underwent six transition cycles. A reduction of the crystallite size accompanied by an increase of the shape anisotropy can be observed, and the crystallites appear to have preferential cleaving planes. In terms of the relative unit-cell parameter variation through the phase transition, the *b* parameter is more impacted (from the neutron diffraction data, 2% variation is detected for the *a* parameter, 8% for the *b* parameter and 5% for the *c* parameter). Hence, the matter displacement accompanying the crystallite reconfiguration through the transition is more important along the *b* axis, and it can be assumed that the cleaving planes would be parallel to the *b* direction, the (*h*0*l*) miller index planes. This hypothesis was confirmed.

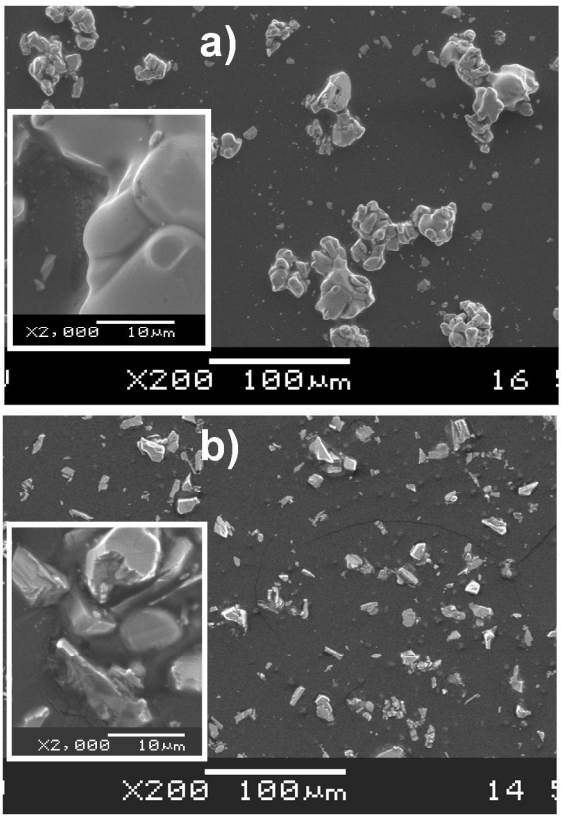

Fig.7. SEM photographs comparing the morphologies of freshly prepared compound (a) and the after 6 phase transition cycles (b).

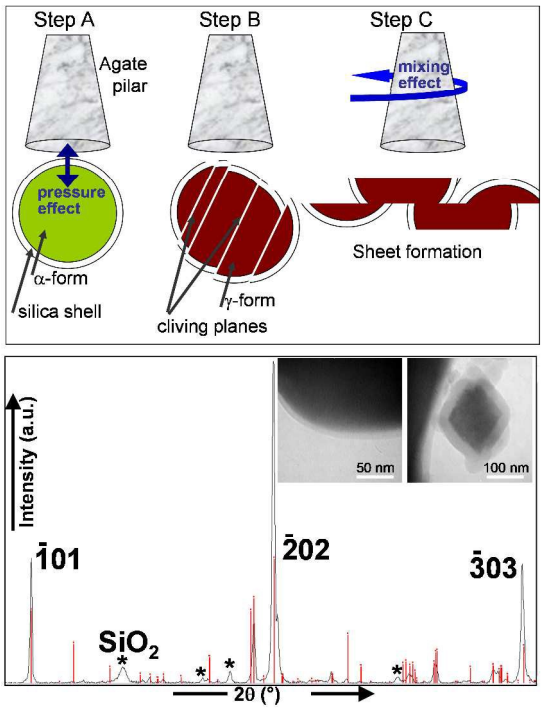

Fig.8. Schematization of the consequence of mechanical grinding on the core-shell powder, X-ray diffraction of the platelet crystals and photographs of the SiO_2 shells on the $CuMo_{0.9}W_{0.1}O_4$ core grains.

To modify the transition temperature, $CuMo_{0.9}W_{0.1}O_4$-SiO_2 core-shells were produced (see [18-21]). SEM images of the core-shell particles are presented in **Figure 8**. Grinding these core-shell particles, which have cores of the high-temperature form, in an agate mortar produces millimeter-scale crystals with thin platelet shape. The X-ray diffraction analyses of one of these crystals show remarkable preferential orientation along the (*-101*) direction. The grinding induces transformation from the high- to low-temperature phase (piezochromic effect), leading to the cleavage of the crystallites along the preferential cleaving planes. In a second step, the affinity of the cleavage planes for each other induces the crystal formation, as represented in **Figure 8**. As illustrated in the α- and γ-form structure projections in **Figure 1**, the (*-101*) planes correspond well to a cutting plane minimizing the number of broken bonds according to surface unit.

Conclusion

$CuMo_{0.9}W_{0.1}O_4$ compound is one typical, even one paroxysmal example of multifunctional materials. In this paper, we have precisely investigated the 1st-order phase transition between its two allotropic forms by neutron diffraction. The experiments have allowed the calculation of the Madelung energies of the two allotropic forms versus the temperature, thus a deep interpretation of the phase transition. Moreover, this transition, associated to a large cell volume variation, is shown to be a "domino-cascade type" transition [33]. Hence, additionally to the piezochromic and thermochromic properties which are associated to a large optical contrast, the extremely brutal behaviour of the transition on the point of view of the crystallite scale, leads to a large thermosalient effect. To the best of our knowledge, this kind of phenomenon on inorganic oxide was never reported in literature.

Notes and references

[a]CNRS, ICMCB, UPR 9048, F-33600 Pessac, France.
[b]Univ. Bordeaux, ICMCB, UPR 9048, F-33600 Pessac, France.
[c]Laboratory for Neutron Scattering and Imaging, Paul Scherrer Institute, 5232 Villigen PSI, Switzerland
*Corresponding authors, email: gaudon@icmcb-bordeaux.cnrs.fr

1 I. Yanase, T. Mizuno and H. Kobayashi, *Ceram. Int.,* 2013, **39**, 2059.
2 T. Asano, T Nishimura, S. Ichimura, Y. Inagaki, T. Kawae, T. Fukui, Y. Narumi, K. Kindo, T. Ito, S. Haravifard and B.D. Gaulin, *J. Phys. Soc. Jap.*, 2011, **80**, 093708.
3 T. Ito, H. Takagi and Asano T., *Chem. Mater.*, 2009, **21**, 3376.
4 D. Hernández, F. Rodríguez, J. Garcia-Jaca, H. Ehrenberg and H. Weitzel, *Physica B*, 1999, **265**, 181.
5 M. Wiesmann, H. Ehrenberg, G. Miehe, T. Peun, H. Weitzel and H. Fuess, *J. Solid State Chem.*, 1997, **132**, 88.
6 N. Kumar, S. Ramaswamy and A. K. Sood, *Phys. Rev. B*, 2011, **80**, 118001.
7 W. Wen, L. Jing, M.G. White, N. Marinkovic, J.C. Hanson and J.A. Rodriguez, *Catal. Lett.*, 2007, **113(1-2)**, 1.
8 H. Ehrenberg, R. Theissmann, Y. Gassenbauer, M. Knapp, G. Wltschek, H.Weitzel, H. Fuess, T. Herrmannsdörfer and D. Sheptyakov, *J. Phys.: Condens. Matter*, 2002, **14**, 8573.
9 F. Rodríguez, D. Hernández, J. Garcia-Jaca, H. Ehrenberg and H. Weitzel, *Phys. Rev. B*, 2000, **61**, 16497.
10 H. Ehrenberg, H. Weitzel, H. Paulus, M. Wiesmann, G. Wltschek, M. Geselle and H. Fuess, *J. Phys. Chem. Sol.*, 1997, **58**, 153.
11 N.N. Leyzerovich, K.G. Bramnik, T. Buhrmester, H. Ehrenberg and H. Fuess, *J. Power Sources*, 2004, **127**(1-2), 76.
12 A. Rabhiou, J. Feist, A. Kempf, S. Skinner and A. Heyes, *Sensor. Actuator. A : Phys.*, 2011, **169(1)**, 18.
13 C.C. Pilgrim, S. Berthier, J.P. Feist, R.G. Wellman and A.L. Heyes, *Surf. Coat. Tech.*, 2012, **209**, 44.
14 C.G. Granqvist, *Solar Energ. Mat. Sol. Cells*, 2007, **91**, 1529.
15 C.B. Greenberg, *Thin Solid Films*, 1994, **251(2)**, 81.
16 N.K. Bourne, J.C.F. Millett and G.T. Gray III, *J. Mater Sci.*, 2009, **44** 3319.
17 Peng Bangyin, Xu Shidang, Chi Zhenguo, Zhang, Xiqi, Zhang Yi and Xu Jiarui, *Prog. Chem.*, 2013, **25**, 1805.
18 L.C. Robertson, L.C., M. Gaudon, S. Jobic, P. Deniard and A. Demourgues, *Inorg. Chem.*, 2011, **50**, 2878.
19 M. Gaudon, A.E. Thiry, A. Largeteau, P. Deniard, S. Jobic, J. Majimel and A. Demourgues, *Inorg. Chem.*, 2008, **47**, 2404.
20 M. Gaudon, P. Deniard, A. Demourgues, A.E. Thiry, C. Carbonera, A. Le Nestour, A. Largeteau, J.-F. Létard and S. Jobic, *Adv. Mat.*, 2007, **19**, 3517.
21 M. Gaudon, C. Carbonera, A.E. Thiry, A. Demourgues, P. Deniard, C. Payen, J.-F. Letard and S. Jobic, *Inorg. Chem.*, 2007, **46**, 10200.
22 P. Fischer, G. Frey, M. Koch, M. Könnecke, V. Pomjakushin, J. Schefer, R. Thut, N. Schlumpf, R.Bürge, U. Greuter, S. Bondt and E. Berruyer, *Physica B*, 2000, **276-278**, 146.
23 J. Rodriguez Carvajal, *Physica B*, 1993, **192**, 55.
24 P.P. Ewald, *Ann. Phys.-New York*, 1921, **64**, 253.
25 F.J. Birch, *J. Geophys. Res.*, 1978, **83**, 1257.
26 S.F. Matar and G. Demazeau, *J. Solid State Chem.*, 2009, **182**, 2678.
27 S.F. Matar, A. Largeteau and G. Demazeau, *Solid State Sci.*, 2010, **12**, 1779.
28 Ž. Skoko, S. Zamir, P. Naumov and J. Bernstein, *J. Am. Chem. Soc.*, 2010, **132**, 14191.
29 S.C. Sahoo, M.K. Panda, N.K. Nath and P. Naumov, *J. Am. Chem. Soc.* 2013, **135**, 13843.
30 S.C. Sahoo, M.K. Panda, N.K. Nath and P. Naumov, *J. Am. Chem. Soc.* 2013, **135**, 12241.
31 K.-J. Fann and H.-C. Hsu, *Adv. Mater. Res.*, 2014, **939**, 430.
32 R. Niemann, U. K. Rdfiler, M.E. Gruner, O. Heczko, L. Schultz and S. Fahler, *Adv. Eng. Mater.*, 2012, **14**, 562.
33 C. Delmas, M. Maccario, L. Croguennec, F. Le Cras and F. Weill, *Nature Mat.*, 2008, **7**(8), 665.